Multi-star calibration in starphotometry

Liviu Ivănescu[1] and Norman T. O'Neill[1]

[1]Département de géomatique appliquée, Université de Sherbrooke, Sherbrooke, QC, Canada

Correspondence: Liviu Ivănescu (Liviu.Ivanescu@usherbrooke.ca)

Abstract. We explored the improvement in starphotometry accuracy using a multi-star Langley calibration in lieu of the more traditional one-star Langley approach. Our goal was a 0.01 calibration-constant repeatability accuracy, at an operational sea-level facility such as our Arctic site at Eureka. Multi-star calibration errors were systematically smaller than single star errors and, in mid-spectrum, approached the 0.01 target for an observing period of 2.5 h. Filtering out coarse mode (super μm) contributions appears mandatory for improvements. Spectral vignetting, likely linked to significant UV/blue spectrum errors at large airmass, may be due to limiting field-of-view and/or sub-optimal telescope collimation. Starphotometer measurements acquired by instruments that have been designed to overcome such effects may improve future star magnitude catalogues and consequently starphotometry accuracy.

1 Introduction

Starphotometry involves the measurement of attenuated starlight in semi-transparent atmospheres as a means of extracting the spectral optical depth, and thereby estimating columnar properties of absorbing and scattering constituents such as aerosols, trace gases and optically thin clouds. Dedicated instrument development had already begun in the late 1950s (Dachs, 1960; Dachs et al., 1966; Dachs, 1966), with increased activity after 2000 (Théorêt, 2003; Gröschke et al., 2009; Pérez Ramírez, 2009) One of the earliest comprehensive investigations of starphotometry errors and their influence on calibration was reported in the astronomical literature by Young (1974). Calibration strategies for retrieving accurate photometric observations in variable optical depth conditions were proposed by Rufener (1964, 1986). Those studies were recently updated and complemented using ~~starphotometer~~ measurements from our High Arctic, sea-level observatory at Eureka, NU, Canada ~~(Ivănescu (2015), Baibakov et al. (2015), Ivănescu et al. (2021))~~(Ivănescu, 2015; Baibakov et al., 2015; Ivănescu et al., 2021), using a commercial spectrometer-based starphotometer[1], attached to a Celestron C11 telescope. This, more recent work, underscored certain challenges in performing calibration at such a high-latitude/low-altitude site. The remoteness of the Eureka site and the significant infrastructure requirements of the starphotometer render calibration campaigns at ~~, say,~~ a dedicated mountain site, onerous. The alternative to a calibration campaign ~~for operational sites~~ (particularly at an Arctic site like Eureka) is to improve on-site calibration methods by overcoming the relatively large optical depth variability ~~at~~ typical for operational sites. Much can be learned by exploring this option at an Arctic location like Eureka (see O'Neill et al. (2016) for a discussion of optical depth variability~~at Eureka~~).

---

[1]Made by Dr. Schulz & Partner GmbH (currently closed).

Star-dependent (one-star) Langley calibration that depends on large airmass variations is the current standard in starphotometry (see ~~Pérez-Ramírez et al. (2008)Pérez-Ramírez et al. (2011)~~Pérez-Ramírez et al. (2008, 2011)). This is mainly due to the limited accuracy of available extraterrestrial star magnitudes ~~Ivănescu et al. (2021)~~(Ivănescu et al., 2021). A good number of High Arctic stars cannot, however, be so calibrated since they do not go through large elevation (i.e. airmass) changes (in the extreme case of a site at the pole, there are no elevation changes). Our goal is to demonstrate that a sub 0.01 optical depth error (partly linked to calibration errors) can be achieved by performing the type of instrument-dependent, star-independent calibration referred to in Ivănescu et al. (2021).

2 Calibration methodology

2.1 Langley calibration

The starphotometer retrieval algorithm is based on extraterrestrial and atmospherically attenuated magnitudes of non-variable bright stars, denoted by M_0 (~~usually provided by a catalog~~provided by the Pulkovo catalogue of Alekseeva et al. (1996)) and M, respectively (see Ivănescu et al. (2021) for ~~the nomenclature details~~a more comprehensive elaboration of this section). Their corresponding ~~(instrument)~~ instrument signals, expressed in terms of ~~a magnitude(logarithmic) formulation, are S_0 and S, respectively~~magnitude, are $S_0 = -2.5 \log F_0$ and $S = -2.5 \log F$, respectively, with F_0 and F being the actual measurements in counts/s. The star-independent conversion factor between the ~~catalog~~ catalogue and instrument magnitudes is (ibid)

$$C = M - S \tag{1}$$
$$C = M_0 - S_0 \tag{2}$$

The C factor accounts for the optical and electronic throughput of the starphotometer, as well as the photometric system transformation between the instrument signal magnitude and the extraterrestrial ~~catalog~~ catalogue magnitude. In terms of magnitude, the Beer-Bouguer-Lambert atmospheric attenuation law is

$$M = M_0 + (m/0.921)\tau \tag{3}$$

where m is the observed airmass and τ is the total optical depth. Inserting equation (1) yields

$$M_0 - S = -\tau x + C \tag{4}$$

where $x = m/0.921$. This expression can be used to retrieve C from a linear regression of $M_0 - S$ versus x, if τ is assumed constant. Such a procedure is referred to as the Langley calibration technique, or Langley plot. In the absence of an accurate M_0 spectrum, equation (2) can be used to transform equation (4) into

$$S = \tau x + S_0 \tag{5}$$

for which a ~~catalog~~ catalogue is no longer required. This linear regression enables the retrieval of S_0 instead of C and thus represents a star-dependent calibration.

55 The right side of equation (4) notably indicates that $M_0 - S$ is star independent: it thus represents a linear regression that any star can contribute to and, accordingly, a framework for multi-star Langley calibration.

3 Calibration errors

3.1 Measurement accuracy

The differential of (rearranged) equation (4) yields the calibration accuracy error

60 $$\delta_C = (\delta_x \tau + x \delta_\tau) - \delta_S + \delta_{M_0} \tag{6}$$

The $(\delta_x \tau + x \delta_\tau)$ component underscores the rationale for performing calibrations at a high altitude site (where τ, δ_τ and $\delta_x \tau$ are typically smaller) and the advantage of maintaining small x in order to minimize the $x \delta_\tau$ contribution to δ_C. The sky stability during the retrieval of C may be monitored by computing τ for each sample, with equation (4). The δ_S error component accounts for any systematic signal changes: optical transmission degradation, misalignment error, star spot vignetting etc. The

65 δ_{M_0} component accounts for any magnitude bias in the bright star ~~catalog~~ catalogue (i.e., ~~it is~~ the average of accuracy-error spectra for all ~~catalog~~ catalogue stars: see Ivănescu et al. (2021) for a detailed discussion of error bias in the ~~catalog stars~~Pulkovo and other catalogues). Because it is a ~~catalog-specific~~ catalogue-specific constant, the optical depth retrieval accuracy will not be affected by its consistent use[2].

3.2 Regression precision

70 A linear regression applied to a plot of $y = M_0 - S$ versus x yields the slope $(-\hat{\tau})$ and intercept $(\hat{C})$ of the Langley equation (4). The regression equation is then $\hat{y} = -\hat{\tau}x + \hat{C}$ and the linear-fit residuals are represented by $r = y - \hat{y}$. The standard error of the regression slope and intercept for a large number of measurements[3] can be expressed as (see, for example, Montgomery and Runger (2011))

$$\sigma_{\hat{\tau}} = \frac{\sigma_{\overline{r}}}{\sigma_x}, \qquad \sigma_{\hat{C}} = \sigma_{\hat{\tau}} \sqrt{\overline{x^2}} \tag{7}$$

75 It should be noted that $\overline{r}$ (the mean of the residual) $= 0$ is a corollary of the linear regression constraints.

The Langley calibration y-axis embodies two independent sets of measurements: N "measurements" of M_0 and n measurements of S. From a pure noise standpoint, the residuals can be represented by an ensemble of individual measurements ($r = (M_0 - S) - (-\tau x + C)$) where each parameter (except C) is subject to noisy variation. Excluding the typically negligible

---

[2]Such an error becomes part of the C value extracted from the Langley calibration of equation (4) and becomes part of the operational retrieval process when equation (4) is inverted to yield individual values of τ.

[3]$n > 10$ where $n = \sum n_i$ (n_i being the number of observations associated with star i).

random errors in x ~~yields~~, it yields[4]

$$80 \quad \sigma_{\overline{r}}^2 = \frac{\sigma_{\epsilon_S}^2}{n} + \underline{\frac{\sigma_{\epsilon_\tau}^2 \, \overline{x^2}}{n}} \, \underwave{\frac{\sigma_\tau^2 \overline{x^2}}{n}} + \frac{\sigma_{\epsilon_{M_0}}^2}{N} = \sigma_{\epsilon_S}^2 + \sigma_{\overline{\tau}}^2 \overline{x^2} + \sigma_{\epsilon_{M_0}}^2 \qquad (8)$$

where the standard error expression for a linear combination of random variables was employed ~~(Barford (1985))~~ (Barford, 1985) . The subscript ϵ represents a single instance of a random (noise) measurement in S, τ or M_0 and σ_ϵ is its zero-mean standard deviation. σ_{ϵ_τ} was replaced by σ_τ because no systematic variation was assumed in τ during the calibration period. ϵ_{M_0} represents the difference between an individual star's M_0 accuracy-errors and the averaged M_0 ~~catalog~~ catalogue bias. The $\sigma_{\epsilon_{M_0}}$

85 term is specific for the use of multiple stars during the calibration.

4 Observing conditions

The assumption of constant τ in time (t) and observational direction (expressed in terms of m) may be problematic over long observation periods and large airmass changes. It is a useful exercise to assess the average time period and airmass range over which a degree of τ constancy (sky stability) is maintained.

90 Variations of a sky instability parameter ($\sigma_{\delta\tau}$) were analyzed using $\delta\tau$ differences for τ measurements acquired during the 2019-2020 season in Eureka. $\delta\tau$ values were placed into (a) fixed Δt bins to generate $\delta\tau$ histograms for high stars (where $\delta\tau = \tau_f - \tau_i$ is computed from a later time (f) relative to an earlier time (i), and (b) fixed Δm bins from high- to low-star m pairs. Since δ of each bin generally come from distinct periods, τ_f and τ_i are expected to be uncorrelated: the τ_i versus τ_f correlation coefficient was determined to be < 0.25 when $\tau_p < 0.1$, $\Delta t < 1\,$h and ~ 0.1 otherwise (see the legend of Figure 1 for

95 the definition of τ_p). This is negligible for the purposes of our analysis and, accordingly, they can be considered as independent variables. The approximation $\sigma_\tau \cong \sigma_{\delta\tau}/\sqrt{2}$ ~~(Soch et al. (2021))~~ (Soch et al., 2021) can accordingly be employed for each Δm or Δt bin.

Those histograms often included anisotropic outliers typical of lognormal τ statistics ~~(Sayer and Knobelspiesse (2019))~~ (Sayer and Knobelspiesse, 2019). A median approach was chosen to render the statistics approximately independent of the

100 outliers: the MAD (Median Absolute Deviation) parameter was employed as a robust measure of histogram width (see equation (1.3) in Rousseeuw and Croux (1993) for MAD details). In order to eventually convert the statistics to those of a normal distribution, an outlier cutoff of $4.5 \cdot \text{MAD}$ was defined[5]. This particular cutoff is equivalent to the classical normal distribution outlier cutoff of 3σ since $\sigma = 1.5 \cdot \text{MAD}$.

Figure 1 shows σ_τ (computed after the outlier cut-off and using the σ_τ approximation given above) as a function of (a) Δt

105 and (b) Δm. It can be shown[6] that a calibration period of 2 h, for which $n \simeq 46$ at the standard sampling rate of starphotometer,

---

[4]Where $\epsilon_{\tau x} = \epsilon_\tau x + \tau\epsilon_x = \epsilon_\tau x$ (since $\epsilon_x = 0$) and the variance of the $\epsilon_\tau x$ product ~~(Goodman (1960))~~ (Goodman, 1960) is $\sigma_{\epsilon_{\tau x}}^2 = \sigma_x^2 \overline{\epsilon_\tau}^2 + \sigma_{\epsilon_\tau}^2 \overline{x}^2 = \sigma_\tau^2 \overline{x^2} \sigma_{\epsilon_{\tau x}}^2 = \sigma_{\epsilon_{\tau x}}^2 = \sigma_x^2 \overline{\epsilon_\tau}^2 + (\sigma_{\epsilon_\tau}^2 \overline{x}^2 + \sigma_{\epsilon_\tau}^2 \sigma_x^2) = \sigma_x^2 \overline{\epsilon_\tau}^2 + \sigma_{\epsilon_\tau}^2 \overline{x^2} = \sigma_x^2 \overline{x^2}$, since $\overline{\epsilon}_\tau = 0$ ~~and~~, $\sigma_{\epsilon_\tau} = \sigma_\tau$ and $\sigma_x^2 = \overline{x^2} - \overline{x}^2$.

[5]A cutoff liberty that we availed ourselves of because one is free to chose the duration of the calibration period and/or to perform outlier filtering prior to Langley regressions.

[6]Using $\sigma_\tau^2 \simeq \sigma_{\hat{C}}^2 n/k_3$ (obtained from equation (B3)), with the terms in S and M_0 neglected, and inserting $\sigma_\tau/\sqrt{n}$ (i.e. $\sigma_{\overline{\tau}}$) into equation (7) and noting that a typical range of $x \in [1.086, 5]$ yields $k_3 \simeq 23$ (see Figure B1).
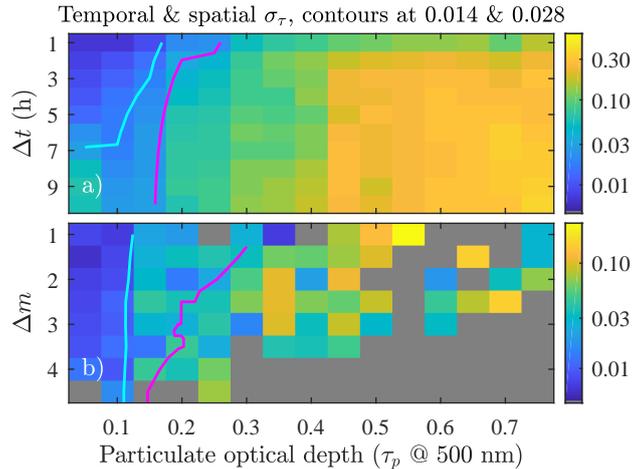
Figure 1. Two dimensional sky instability (σ_τ) patterns for the 2019-2020 season at Eureka. The colour coded σ_τ values are computed relative to a reference τ value but plotted as a function of its associated particulate optical depth ($\tau_p = \tau - \tau_m$, where τ_m is the molecular scattering optical depth) and a) time difference (Δt), or b) air mass difference (Δm). The magenta and purple curves represent the column-wise averaged $\sigma_\tau = 0.014$ and 0.028 contour lines. There was much more data associated with Δt than with Δm bins (i.e. more robust bin statistics are expected in the former case). Note that Δm and Δt were chosen to be positive.
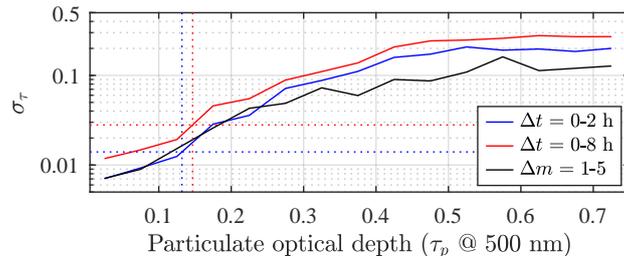
Figure 2. σ_τ vs τ_p for the three calibration scenarios defined.

yields $\sigma_\tau \simeq 1.4\sigma_{\hat{C}}$. This means that the calibration error ($\sigma_{\hat{C}}$) is limited to < 0.01 only if $\sigma_\tau < 0.014$. An 8-h observing period enables a more generous limit of $\sigma_\tau < 0.028$ to achieve the same calibration precision. Contour curves of $\sigma_\tau = 0.014$ and 0.028 are superimposed on Figure 1.

Figure 2 shows the σ_τ variability estimation for the 2-h "fast" and the 8-h "long" calibration periods, as well as a third scenario with $\Delta m = 1$ to 5. The three curves represent the standard deviation (after cut-off) of the corresponding range-aggregated data. They tend to converge with decreasing τ_p: the 2-h and 8-h σ_τ values of 0.014 and 0.028 correspond to τ_p values of 0.13 and 0.15, respectively (blue and red dashed vertical lines defined by the intersection with the corresponding horizontal 0.014 and 0.028 lines). The cases $\tau_p \leq 0.13$ and 0.15 were labeled as "clear-sky" conditions because of their tendency to promote calibration stability. Their corresponding clear-sky statistics are presented in appendix A.
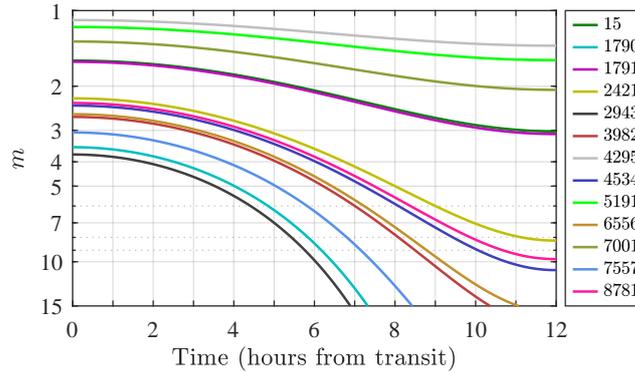
Figure 3. Airmass versus time past the transit for the bright stars observable at Eureka (identified by their HR ~~catalog~~ catalogue index). The transit of a given star occurs when it crosses the local meridian (minimum airmass).

Many high Arctic stars are circumpolar (i.e. they never set) and thus their airmass range is limited. Figure 3 shows airmass variation as a function of time past the transit for our dataset of the 13 brightest (and stable) stars at Eureka. A well defined separation is notable between high stars ($m(12h) < 3.1$) and low stars ($m(0h) > 2.2$). A large airmass range is clearly only available for the low stars (i.e. about 2/3 of our Eureka bright-star dataset). However, star vignetting, due to turbulence-inducing star-spot expansion beyond the boundaries of the Field of View (FOV), may affect the optical throughput of the Eureka system at $m > 5$ ~~(Ivănescu et al. (2021))~~(Ivănescu et al., 2021). This type of airmass constraint, combined with the low star constraints of Figure 3, results in only moderate Δm excursions (at the expense of substantial Δt) if only a single star is employed in a Langley type calibration. A multi-star calibration can be exploited to mitigate such Δm and Δt limitations.

5 Multi-star calibration

This type of calibration exploits a singular advantage of starphotometry over moonphotometry and sunphotometry: the capability of employing multiple extraterrestrial light sources in a relatively short period of time. In comparison with a C-determining Langley calibration using one star, the multi-star approach enables a synergistic Langley calibration that employs several stars exhibiting a wide range of airmass values over a significantly shorter period of time.

One- and multi-star Langley calibrations acquired with the Eureka starphotometer on 2019/12/07 and 2020/01/10, respectively, are shown in Figure 4. The observations for $x > 5$ were carried out to highlight any vignetting effect due to the aforementioned star-spot expansion. The one-star case (small black dots and their associated "1-lin" regression line) are the results for the low Procyon star (HR 2943, spectral type F5V). Its colder temperature ensures a near infrared (NIR) brightness that is larger than all the other bright stars of Figure 3[7]. That reason aside, it is also, arguably, the most optimal one-star Langley-regression choice since no other Figure 3 bright star can duplicate its large and rapid airmass change (c.f. the lowest black curve).

---

[7] The other bright stars, being of similar A-B type ~~(ibid)~~(Ivănescu et al., 2021), ~~generally~~ exhibit lower signal-to-noise (SNR) in the NIR.
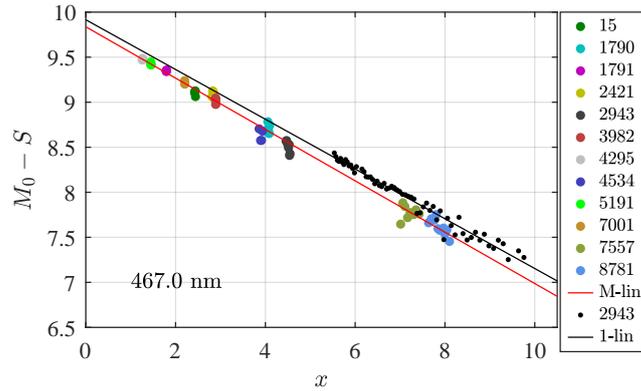
Figure 4. One- and multi-star Langley calibrations (both lasted about 2.5 h, see appendix A). The one-star and multi-star measurement points are represented, respectively, by small black dots and large solid-colored circles, while their linear regression fits appear as solid lines (1-lin and M-lin, respectively). Each point represents an average of five 6 s exposures. Each star is identified by their HR IDs ~~(Ivănescu et al. (2021))~~ (Ivănescu et al., 2021).

5.1 Calibration precision

The resulting one- and multi-star $\hat{\tau}$ spectra (each spectral point representing a linear-regression Langley slope) are shown in Figure 5a. Their associated precision errors ($\sigma_{\hat{\tau}}$) of equation (7) are shown in Figure 5b. One should note that the estimated multi-star error is substantially and consistently smaller than that of the one-star calibration. The $\hat{C}$ and $\sigma_{\hat{C}}$ spectra from the Langley regressions are shown in Figure 6a and Figure 6b, respectively. The $\sigma_{\hat{C}}$ values are, in the multi-star case, significantly smaller and closer to the 0.01 target.
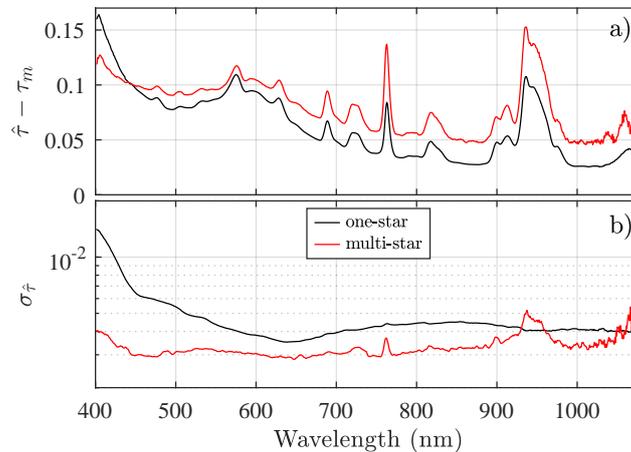
Figure 5. a) One- and multi-star Langley-regression slopes (expressed as $\hat{\tau}_p = \hat{\tau} - \tau_m$). b) $\sigma_{\hat{\tau}}$ values derived from eq. (7).
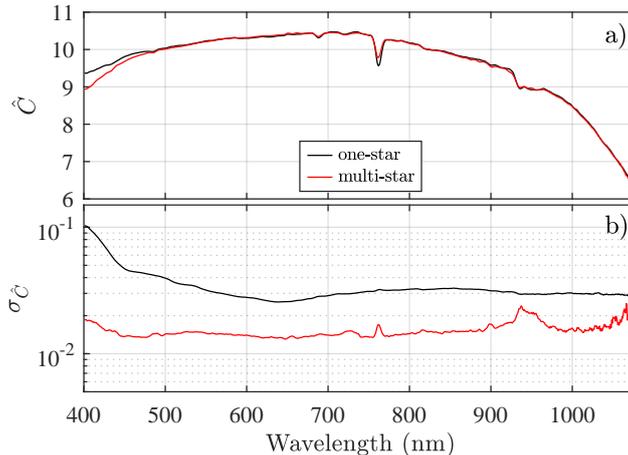
Figure 6. a) $\hat{C}$ retrieved from the one- and multi-star Langley calibrations. b) $\sigma_{\hat{C}}$ values computed using equation (7).

The generally smaller $\sigma_{\hat{\tau}}$ values of the multi-star case are partly attributable to the one-star case being limited to a relatively smaller x range (i.e. smaller σ_x in equation (7)) while the smaller $\sigma_{\hat{C}}$ values are partly attributable to the smaller $\sigma_{\hat{\tau}}$ values and the ~~generally~~ lower values of ~~x~~ $\overline{x^2}$ (c.f. equation (7~~b~~)). The $\sigma_{\hat{C}}$ increases in the ultraviolet (UV) and NIR are discussed in subsection 6.2. The peak around 940 nm is likely associated with a faint and noisy star signal induced by strong atten-
uation in the water vapour absorption band, coupled with the non-linear nature of the optical depth in that spectral region ~~(Pérez-Ramírez et al. (2012))~~(Pérez-Ramírez et al., 2012).

5.2 Repeatability

The robustness of the $\sigma_{\hat{C}}$ spectra of Figure 6b and the impact of potential systematic errors can be investigated with repeatability experiments. The $\hat{C}$ spectra employed to produce the standard deviations[8] shown in Figure 7 were derived from three one-star and three multi-star Langley calibrations that were well separated in time (i.e., they were optically independent in terms of any significant correlations between the τ_p variations of each period) and nearly satisfied the clear-sky calibration constraints of section 4. The Figure 7 error spectra are, with the exception of larger differences in certain spectral regions, roughly coherent with the Figure 6b spectra (including the fact that the one-star errors are significantly larger than the multi-star errors).

6 Regression error discussion

6.1 Data processing

Figure 8 shows dual wavelength (400 and 1000 nm) regression tests for two of the three one-star calibrations of the previous section (two of the three dates given in the legend of Figure 7 for the HR 2943 star) plus a third hotter star (HR 3982, spectral

---

[8]Standard deviations that, we would argue, are also standard errors (each of the three $\hat{C}$ spectra that were averaged were more akin to means).
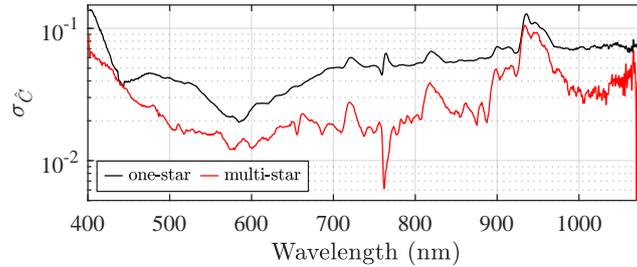
Figure 7. $\sigma_{\hat{C}}$ curves derived for three one-star Langley calibrations acquired using the Procyon (HR 2943) star on 2019/12/07, 2020/01/05 and 2020/01/16, as well as three multi-star calibrations acquired on 2018/03/10, 2019/12/07 and 2020/01/10. These spectra are generally similar to Figure 6b results.

type B7) that was specifically chosen to better understand the influence of temperature-driven spectral differences in the target star. The smaller regression-slope and point dispersion about the HR 3982 regression line, compared with the two HR 2943

160 cases, is noticeable at both wavelengths (notably at 1000 nm) and is an indicator of generally clearer sky conditions.

The C values retrieved from linear regressions over an increasing x range in Figure 8 (from the smallest x value to an artificial maximum of x_{max}) are plotted in Figure 9. The damping out of regression noise and the asymptotic approach to the horizontal pan-x regression value as x_{max} increases can be readily observed in all three plots. ~~One-star calibrations at two spectrally distinct channels (400 and 1000 nm) for different dates and stars. The black lines represent the full regression line~~

165 ~~for all data points over the entire x range. Star measurements for the a) and b) cases started at the smallest x values, while the c) case measurements began at the largest x value. The solid (varying) curves were generated by averaging $(M_0 - S)$ over $\Delta x = 1.5$ sliding windows. The three colored (dotted) vertical lines correspond to the colors of the three x_{max} cases of Figure 10.~~

The corresponding slope-derived τ_p spectra are shown in Figure 10 for three x_{max} cases (the three colored spectra were

170 derived for x_{max} values corresponding to the matching colors of the three vertical lines in Figure 8 and Figure 9). The x-dependent regression error dynamics are investigated in appendix C. The next subsection describes potential competing causes of C variations and makes a link to τ_p errors[9].

6.2 Regression error interpretation

The sky instability plots of Figure 1 show that the standard deviation of the optical depth increases with time and airmass

175 separation between any two stars (this applies equally well to the variation between two positions of the same star). A systematic optical depth drift during the calibration leads to a common-signed bias (positive or negative) of the regression slope and the calibration value, relative to drift free conditions. Figure 10a and 10b show spectrum-wide τ_p reduction as x_{max} and calibration time increase. This suggests spatial and/or temporal sky transparency instability during calibration. Such rapid and spectrally

---

[9]The strong, positive correlation between C and τ_p and between their errors is the result of variations in the regression lines being effectively driven by rotations about a cluster of pivot points whose x position changes little.
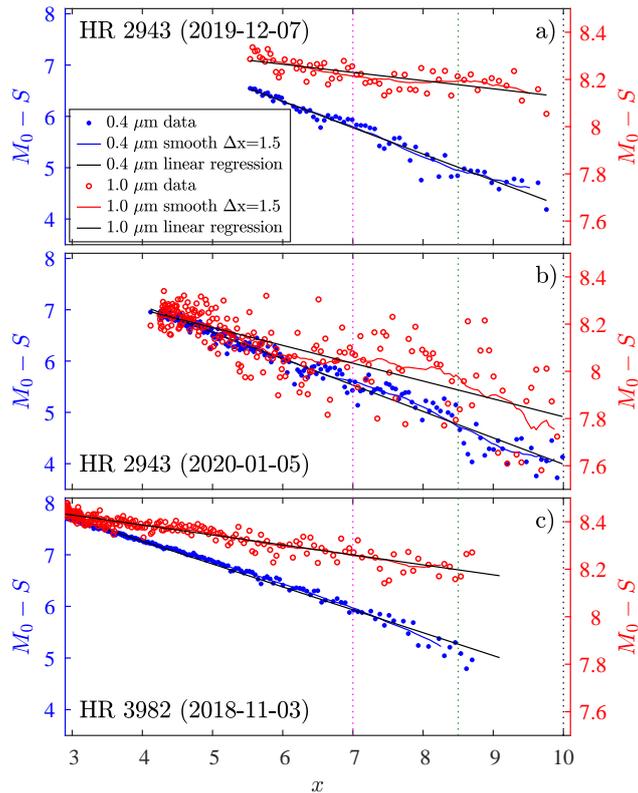
Figure 8. One-star calibrations at two spectrally distinct channels (400 and 1000 nm) for different dates and stars. The black lines represent the full regression line for all data points over the entire x range. Star measurements for the a) and b) cases started at the smallest x values, while the c) case measurements began at the largest x value. The solid (varying) curves were generated by averaging $(M_0 - S)$ over $\Delta x = 1.5$ sliding windows. The three colored (dotted) vertical lines correspond to the colors of the three x_{max} cases of Figure 10.

neutral variation is consistent with the domination of coarse mode (super μm) particles: a (post cloud-screened) mode that is
180   mostly dominated by spatially homogeneous cloud particles at Eureka ~~(O'Neill et al. (2016))~~(O'Neill et al., 2016). The near-superposition of all τ_p spectra above 500 nm in Figure 10c indicates stable transparency that is characteristic of a cloud-free atmosphere dominated by fine-mode (sub μm) particles. A number density induced drift of similar fine-mode aerosol particles will generate spectrally independent variations in $\Delta \tau_p / \tau_p$: the larger τ_p value (corresponding to the larger absolute difference in the blue/UV part of the spectrum) could explain the increasingly larger UV deviations (such as between the magenta and
185   black/green curves in Figure 10c).

    The two bullet-lists below summarize the specific processes that can lead to variations of calibration slope (τ_p) and intercept (C), traceable to real or apparent optical depth variations.

Instances of τ_p and C overestimation
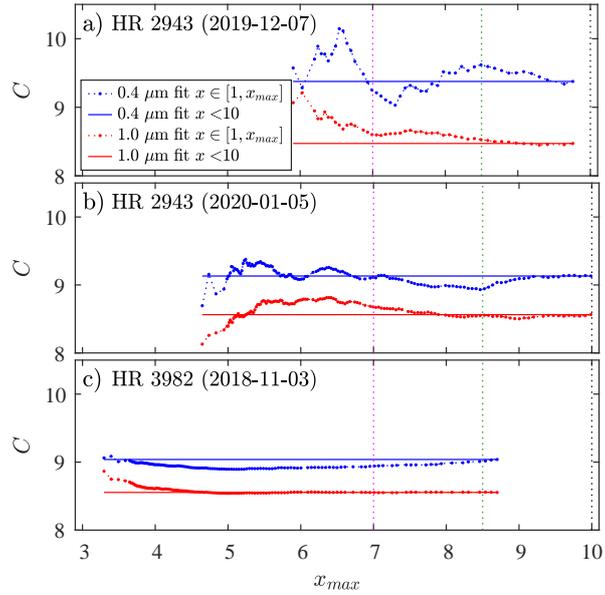
Figure 9. C values retrieved from linear regressions over an increasing x range, i.e. from the smallest x to an increasing x_{max} for all the cases plotted in Figure 8. The horizontal reference lines represent regressions over the entire x range (the solid lines of Figure 8), while the three colored (dotted) vertical lines correspond to the colors of the three x_{max} cases of Figure 10.
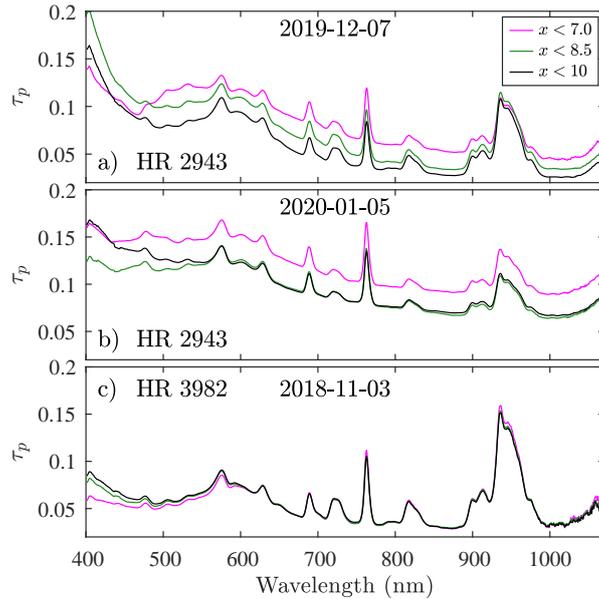
Figure 10. Optical depth (slope) spectrum retrieved from calibration performed at different x ranges.

- A systematic coarse-mode τ_p increase (as described above) can have a dramatic spectrum-wide effect: flagging and discarding such measurements is, accordingly, essential. A fine-mode τ_p increase will predominantly affect the UV/blue part of the spectrum.

- Recent tests indicate that the optical collimation of the Eureka Celestron C11 telescope requires correction. Mis-collimation is responsible for a significant part of the star spot size reported in Ivănescu et al. (2021). Correcting the attendant vignetting problem (whose consequence is a decreased star flux and apparent increase in τ_p) may enable reliable measurements at x values well above the limit of $x \simeq 5$ reported by Ivănescu et al. (2021).

- The angular star spot size (ω), being proportional to $\lambda^{-1/5}x^{3/5}$ (equations 4.24, 4.25 and 7.70" of Roddier (1981)), effectively leads to spectrally dependent vignetting (i.e. apparent τ_p and C increase) as a function of x: an increase in x from 7 to 9.5 would be equivalent to 20% of ω increase for a spectral change from 400 to 1000 nm. This coupled spectral and airmass vignetting influence is consistent with Figure C1 with the blue (0.4 μm) curve increasing at $x \simeq 7$ while the increase of the red (1.0 μm) curve occurs only at $x > 9$. This dynamic potentially dominates the large UV/blue errors seen in Figure 7 and Figure 10.

- Noisier star spots, attributable to increased turbulence and scintillation at large x, may induce larger centering errors and exacerbate apparent increases in τ_p and C due to vignetting.

Instances of τ_p and C underestimation

- A systematic τ_p decrease during the calibration period (notably when the calibration starts at large τ_p).
- Weak signals, usually at large x and notably for hot stars in the NIR, may lead to sensitivity loss due to ADC (analog to digital conversion) limitations and attendant slope and intercept (τ_p and C) reductions.

These factors contribute to Figure 10 τ_p dynamics and likely relate to the one-star $\sigma_{\hat{C}}$ spectra shown in Figure 7. A very similar spectrum is indeed observed in the case of one faint star at large airmass (Figure 11). Such spectral dynamics, possibly dominated by the aforementioned spectral influence of vignetting, are also likely related to the similar M_0 bias spectra shown in Figures 4 and 11 of Ivănescu et al. (2021). The identification of the M_0 bias source is of paramount importance, as it may guide strategical observation choices made to improve the accuracy of future star catalogues. The error envelopes about the M_0 bias (quantified in Figure 12) add an additional, roughly flat spectral component (in spectral regions other than those ~~those~~ that are dominated by H-absorption bands).

The smoother NIR errors in the one-star case (comparing the black one-star curve with the red multi-star curve of Figure 5a for $\lambda > 1050$ nm) is likely due to the strong NIR signal of the much colder Procyon star. One can take advantage of this effect and develop an observing strategy that avoids using faint stars at large airmass ~~at~~ in Eureka and still employ 12 catalogue stars at $x < 8$ in a multi-star calibration lasting 2.5 h (c.f. Figure A2). The star selection operation for a given multi-star calibration should also include a random airmass selection to mitigate accuracy errors attributable to systematic optical depth variations (as an alternative to the Rufener (1986) method). Mitigation of both, starlight reduction impacts at large airmass and systematic optical depth variations, is a singular advantage of the multi-star vs one-star calibration.
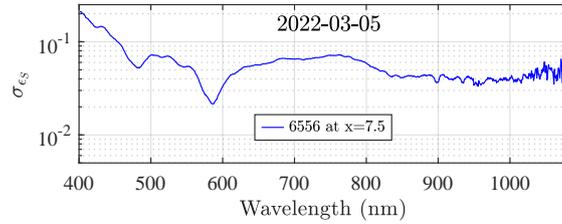
Figure 11. Standard deviation of S magnitude measurements at large airmass for a faint catalogue star (HR 6556, V=2.08).
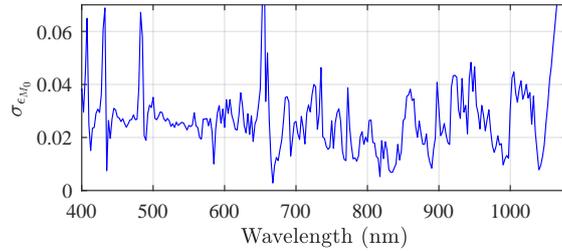
Figure 12. Standard deviation of M_0 errors deduced from the error bars of Figure 4 in Ivănescu et al. (2021).

7 Conclusions

It was determined that no Eureka star movement satisfied an optimal sky-transit scenario of maximum possible airmass range within the constraint of ~~x being $\lesssim 5$~~ $x < 5$. The solution to this intrinsic shortcoming of a High Arctic site is to perform multi-star calibrations: this approach incorporates the fundamental advantage of reducing the calibration period and thus minimizing optical depth variability. It is, by its very nature, a calibration that enables the retrieval of a star-independent calibration parameter.

Multi-star calibration repeatability errors ($\sigma_{\hat{C}}$) were systematically smaller than the single star errors and, in the central part of the spectrum, approached the target value of 0.01 for an observing period of 2.5 h. Those errors were partly affected by less than optimal clear sky conditions (notably in the presence of cloud), with τ_p slightly larger than the recommended "clear-sky" value of 0.13: c.f. section 4 and appendix A). Coarse mode filtering algorithms, that ideally eliminate all influences of coarse mode optical depth specifically in a calibration scenario, are necessary to ensure the best calibration[10]. Large UV and NIR errors can be reduced by avoiding faint stars at large x and by improving the current telescope collimation. The mitigation of mis-collimation problems can, in the short term, be affected by a constraint of $x < 7$. This can be achieved at Eureka by employing 12 constrained-magnitude stars over a 3 h calibration period (c.f. appendix A). A constraint of ~~$\tau_p < 0.13$~~ $\tau_p < 0.13$ may bring the calibration errors in the blue-to-red spectral range closer to the 0.01 target, with the remaining UV and NIR spectral regions being subject to the influence of M_0 errors.

---

[10]Clouds are usually the dominant coarse mode component but coarse mode aerosols can have diverse effects which are typically, but not always, minor.

In summary, the advantages of multi-star versus one-star calibration, are star-independent calibration, faster coverage of larger airmass ranges, more calibration opportunities and star selection capability for both mitigating the impact of starlight reduction with increasing airmass and systematic optical depth variations. These singular benefits were shown to override the drawbacks of specific star catalogue errors (i.e. the multi-star calibration performs better than the one-star case, even if the former is uniquely affected by M_0 errors). Further improvement will only be achieved by developing a more accurate extraterrestrial star-magnitude ~~catalog~~catalogue: their UV/blue errors, likely linked to large-x spectral vignetting or fine mode aerosol variations, are endemic to current ground-based star catalogues. This improvement may be affected from a space-borne platform or at a high-elevation observatory (the primary goal being to reduce turbulence-induced star-spot size and optical depth variability). The use of a large aperture telescope (limiting scintillation and low-starlight measurement errors) and a larger FOV instrument (less prone to vignetting) will, in general, provide better results.

Code and data availability. Final MATLAB code and data employed in the generation of the figures is freely available (see Ivănescu (2023)).

Appendix A: Calibration opportunities

Figure A1a shows the τ_p histogram for data acquired during the 2019-2020 observing season at Eureka[11]. The blue and red vertical lines respectively indicate the clear-sky cutoff values of 0.13 and 0.15 determined in section 4 for the 2-h and 8-h calibrations. Operational conditions occurred 37% of the time (i.e. those periods of time when measurements were not impeded by persistent thick clouds or the performance of maintenance tasks). A frequency curve of clear-sky periods (a period for which all τ_p values are less than the cutoff value) is presented in Figure A1b. Measurements acquired during 2-h and 8-h clear-sky periods represented, respectively, 35.5% and 39% of all measurements. These numbers, transformed into an estimation of clear-sky fraction of the total measurement time, yield values of 13% and 14% of the total contiguous seasonal time ($0.37 \cdot 0.355$ and $0.37 \cdot 0.39$, respectively). Since the measurement season is ~160 days (or ~5.3 months[12]) and given that there were 246 clear-sky periods of 2 h with $\tau_p < 0.13$, one may expect 46 such calibration periods per month. There were, on the other hand, 29 clear sky periods of 8 h with $\tau_p < 0.15$ (or ~5.5 per month). If a calibration can be successfully completed in ~2 h then there is a significantly larger probability-of-occurrence incentive for doing so.

The weakening of star signals with increasing airmass will progressively impact calibration quality. Figure A2 shows the availability of catalogue stars for a multi-star calibration over Eureka as a function of calibration period and maximum airmass. A calibration can, for example, be carried out in 2 h with only 11 stars of our 13 star dataset (Figure 3). A 12 star calibration can be carried out only if $x < 9.5$, or if the calibration period is > 2.5 h.

---

[11]We could speculate that the two histogram peaks near τ_p values of 0.1 and 0.16 are associated with the background fine mode optical depth and the enhanced fine mode optical depth incited by the presence of wind blown seasalt ~~(O'Neill et al. (2016))~~(O'Neill et al., 2016).

[12]Which we pragmatically define as the number of nights for which reliable measurements can be carried out for ≥ 30 minutes.
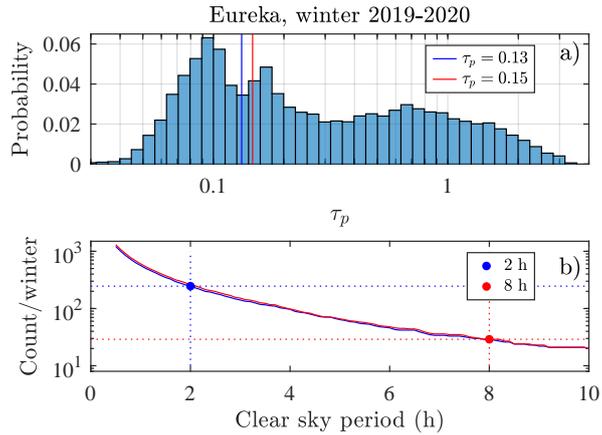
Figure A1. τ_p histogram for measurements acquired during the 2019-2020 observing season at Eureka (total of 25914 measurements). The blue and red vertical lines are the clear-sky cutoff values of 0.13 and 0.15 determined in section 4. The probability is normalized so that its sum is unity (a). Frequency of occurrence vs duration of clear-sky periods (b).
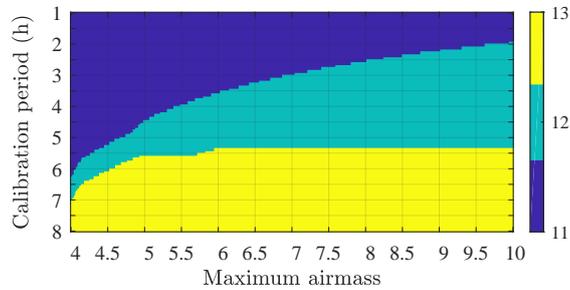
Figure A2. Number of available catalogue stars for a multi-star calibration, during a 24 h period. The following constraints were employed in generating the tri-color contours: at least one star at $x < 1.2$, exclusion of any star of visual magnitude $V > 1.5$ for $x > 6$, as well as $V > 2$ at $x > 5$.

265 **Appendix B: Relative importance of component errors**

From equation (7) and (8) one gets the error propagation into the τ Langley retrieval

$$\sigma_{\hat{\tau}}^2 = \frac{\sigma_{\hat{\tau}}^2}{\sigma_x^2} = \frac{1}{\sigma_x^2}\left(\sigma_{\epsilon_S}^2 + \overline{x^2}\sigma_{\overline{\tau}}^2 + \sigma_{\epsilon_{M_0}}^2\right) \tag{B1}$$

$$\sigma_{\hat{\tau}}^2 = k_1\sigma_{\epsilon_S}^2 + k_2\sigma_{\overline{\tau}}^2 + k_1\sigma_{\epsilon_{M_0}}^2, \text{with } k_1 = \frac{1}{\sigma_x^2}, k_2 = \frac{\overline{x^2}}{\sigma_x^2} \tag{B2}$$

Error propagation into the calibration constant (C) retrieval is, in a similar fashion, expressed as

$$\sigma_{\hat{C}}^2 = \sigma_{\hat{\tau}}^2 \overline{x^2} = \frac{\overline{x^2}}{\sigma_x^2}\left(\sigma_{\bar{\epsilon}_S}^2 + \overline{x^2}\sigma_{\overline{\tau}}^2 + \sigma_{\bar{\epsilon}_{M_0}}^2\right) \tag{B3}$$

$$\sigma_{\hat{C}}^2 = k_2\sigma_{\bar{\epsilon}_S}^2 + k_3\sigma_{\overline{\tau}}^2 + k_2\sigma_{\bar{\epsilon}_{M_0}}^2, \text{with } k_3 = \frac{\overline{x^2}^2}{\sigma_x^2} \tag{B4}$$

The coefficients k_1, k_2 and k_3 are displayed in Figure B1b, c and d, respectively, for the x protocols of Figure B1a. The blue curve shows uniformly distributed values of x, while the red curve shows a more realistic observing configuration of constant time intervals[13]. In order to investigate more practical (smaller) ranges, the working range is incrementally truncated from both, the right and left (the solid and dashed curves, respectively). The focus is on two particular ranges: $x < 5$ (red-filled circles), where $k_1 \simeq 1.2$, $k_2 \simeq 5.3$ and $k_3 \simeq 23$ (approximately-stabilized for $X \gtrsim 4$), and $x > 5$ (open red circles), where $k_1 \simeq 0.5$, $k_2 \simeq 25$ and $k_3 \simeq 1250$ (i.e. > 50 times greater than that for $x < 5$). This strong weighting towards large x drives the standard error in C. The term $\sigma_{\bar{\epsilon}_S}$ is typically $\sim \sigma_{\overline{\tau}}$, which is, in turn $\sim \sigma_{\bar{\epsilon}_{M_0}}$ Ivănescu et al. (2021). The $\sigma_{\hat{\tau}}^2$ term may, accordingly, tend to dominate the $\overline{\epsilon_S}^2$ and $\sigma_{\bar{\epsilon}_{M_0}}^2$ terms in equation (B3)[14] and thus the $\sigma_{\hat{C}}$ calibration error.

Appendix C: Error discussion supplement

The C values, derived from tangents applied to the Figure 8 solid curves (the means of a $\Delta x = 1.5$ sliding window), are plotted in Figure C1. The objective of this plot is to highlight more robust (lower frequency) C variations (and thus C errors) as a function of x. The 400 nm C values are relatively stable up to $x \simeq 7$ to 7.5 where they are subject to a large increase. The 1000 nm C pattern is similar with an increase beginning at $\simeq 9$ (observations that are roughly consistent with the vignetting arguments of subsection 6.2).

Author contributions. Liviu Ivănescu: conceptualization, methodology, data curation, software, formal analysis, investigation, writing original draft. Norman T. O'Neill: validation, writing, review and editing, supervision, funding acquisition.

Competing interests. No competing interests are present.

Acknowledgements. This work was supported by CANDAC (the Canadian Network for the Detection of Atmospheric Change) via the NSERC PAHA (Probing the Atmosphere of the High Arctic) project, by the NSERC CREATE Training Program in Arctic Atmospheric Science, as well as by the grant 21SUASACOA and the FAST program of the Canadian Space Agency (CSA). Finally we also gratefully acknowledge the support of the CANDAC operations staff at Eureka for their numerous troubleshooting interventions.

---

[13]Both conditions apply to a star crossing the meridian at zenith.

[14]Since, as per Figure B1e, $4 < \overline{x^2} < 50$.
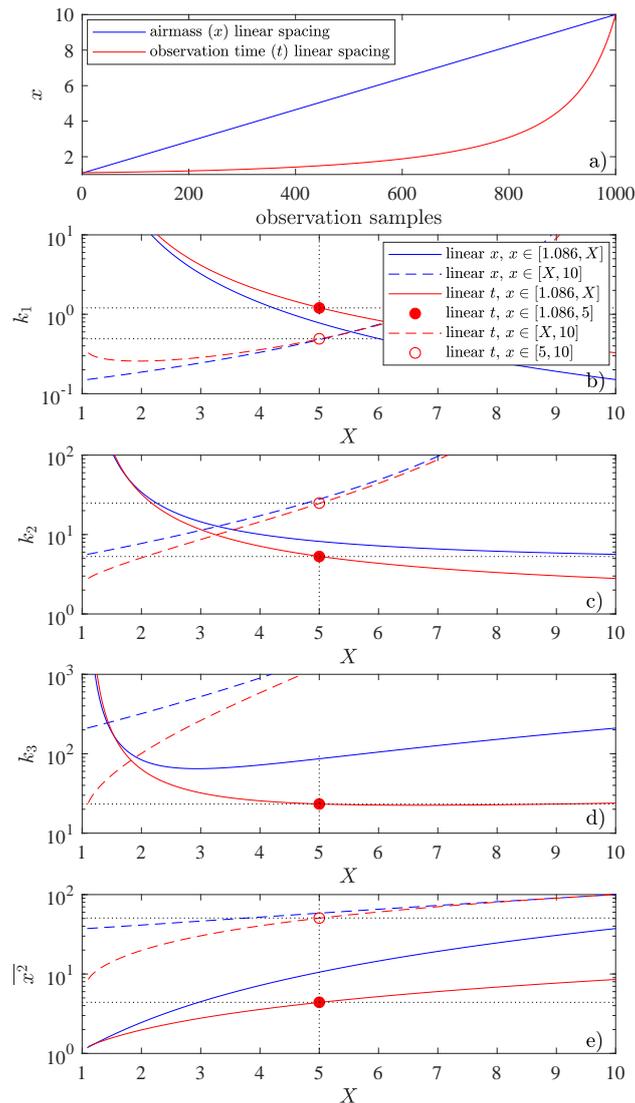
Figure B1. Variation of x as a function of the number of observation samples for measurements made in equal increments of x (blue curve) and equal increments of time (red curve) (a). The next three panels show the x dependent variation of k_1, k_2 and k_3 (see text for more details). The legend in panel (b) applies to all the subsequent panels. Panel (e) shows $\overline{x^2}$, the σ_{τ}^2 to $\sigma_{\hat{C}}^2$ conversion factor of equation (B3).

References

Alekseeva, G. A., Arkharov, A. A., Galkin, V. D., Hagen-Thorn, E., Nikanorova, I., Novikov, V. V., Novopashenny, V., Pakhomov, V., Ruban, E., and Shchegolev, D.: The Pulkovo Spectrophotometric Catalog of Bright Stars in the Range from 320 TO 1080 NM, Baltic Astronomy, 5, 603–838, http://adsabs.harvard.edu/abs/1997BaltA...6..481A, 1996.

295
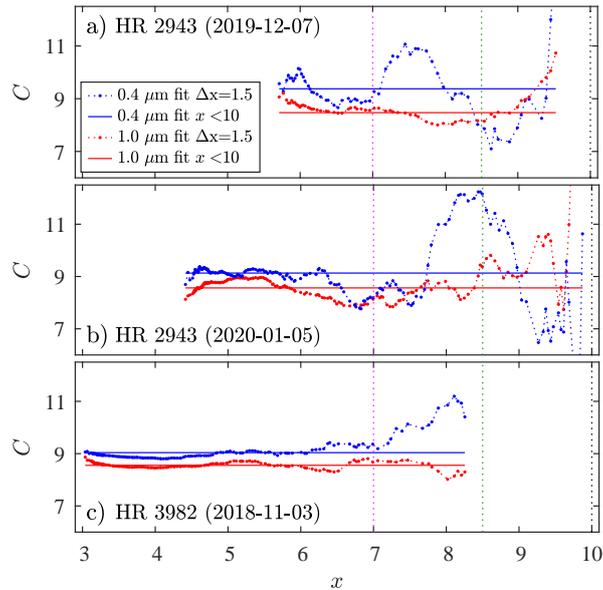
Figure C1. The variable curves show the calibration (C) variation for regressions associated with the low frequency (sliding window) curves of Figure 8. The horizontal lines correspond to the single C value retrieved from the full (pan-x) regression lines of Figure 8, while the three colored (dotted) vertical lines correspond to the colors of the three x_{max} cases of Figure 10.

Baibakov, K., O'Neill, N. T., Ivănescu, L., Duck, T. J., Perro, C., Herber, A. B., Schulz, K.-H., and Schrems, O.: Synchronous polar winter starphotometry and lidar measurements at a High Arctic station, Atmospheric Measurement Techniques, 8, 3789–3809, https://doi.org/10.5194/amt-8-3789-2015, 2015.

300   Barford, N.: Experimental measurements: precision, error and truth, John Wiley and Sons Ltd., Chichester, 2nd edn., www.worldcat.org/oclc/11622295, 1985.

Dachs, J.: Lichtelektrische Sternphotometrie und Farbenindexmessungen durch Zahlung von Photoelektronen, Ph.D. thesis, Tübingen University, https://www.worldcat.org/title/249623335, 1960.

Dachs, J.: Ein Photoelektronen zählendes Sternphotometer, Astronomische Nachrichten, 289, 129–138,
305   https://doi.org/10.1002/asna.19662890305, 1966.

Dachs, J., Haug, U., and Pfleiderer, J.: Atmospheric extinction measurements by photoelectric star photometry, Journal of Atmospheric and Terrestrial Physics, 28, 637–649, https://doi.org/10.1016/0021-9169(66)90077-8, 1966.

Goodman, L. A.: On the Exact Variance of Products, Journal of the American Statistical Association, 55, 708–713, https://doi.org/10.1080/01621459.1960.10483369, 1960.

310   Gröschke, A., Herber, A. B., Schrems, O., Schulz, K.-H., and Gundermann, J.: Development and application of a new star photometer for measuring aerosol optical depth at harsh environments, in: EGU General Assembly 2009, p. 10485, Vienna, https://meetingorganizer.copernicus.org/EGU2009/EGU2009-10485.pdf, 2009.

Ivănescu, L.: Une application de la photométrie stellaire à l'observation de nuages optiquement minces à Eureka, NU, Master in science thesis, UQAM, www.archipel.uqam.ca/id/eprint/8417, 2015.

315 Ivănescu, L.: Multi-star calibration in starphotometry, code and data, https://doi.org/10.5281/zenodo.7975245, 2023.

Ivănescu, L., Baibakov, K., O'Neill, N. T., Blanchet, J.-P., and Schulz, K.-H.: Accuracy in starphotometry, Atmos. Meas. Tech., 14, 6561–6599, https://doi.org/10.5194/amt-14-6561-2021, 2021.

Montgomery, D. C. and Runger, G. C.: Applied Statistics and Probability for Engineers, John Wiley and Sons, Inc., 5 edn., http://www.worldcat.org/oclc/28632932, 2011.

320 Oh, Y.-L.: Retrieval of Nighttime Aerosol Optical Thickness from Star Photometry, Atmosphere, 25, 521–528, https://doi.org/10.14191/Atmos.2015.25.3.521, 2015.

O'Neill, N. T., Baibakov, K., Hesaraki, S., Ivănescu, L., Martin, R. V., Perro, C., Chaubey, J. P., Herber, A. B., and Duck, T. J.: Temporal and spectral cloud screening of polar winter aerosol optical depth (AOD): impact of homogeneous and inhomogeneous clouds and crystal layers on climatological-scale AODs, Atmospheric Chemistry and Physics, 16, 12 753–12 765, https://doi.org/10.5194/acp-16-12753-325 2016, 2016.

Pérez Ramírez, D.: Caracterización del aerosol atmosférico en la ciudad de Granada mediante fotometría solar y estelar, Ph.D. thesis, Granada, http://hdl.handle.net/10481/5628, 2010.

Pérez-Ramírez, D., Aceituno, J., Ruiz, B., Olmo, F. J., and Alados-Arboledas, L.: Development and calibration of a star photometer to measure the aerosol optical depth: Smoke observations at a high mountain site, Atmospheric Environment, 42, 2733–2738, 330 https://doi.org/10.1016/j.atmosenv.2007.06.009, 2008.

Pérez-Ramírez, D., Lyamani, H., Olmo, F. J., and Alados-Arboledas, L.: Improvements in star photometry for aerosol characterizations, Journal of Aerosol Science, 42, 737–745, https://doi.org/10.1016/j.jaerosci.2011.06.010, 2011.

Pérez-Ramírez, D., Navas-Guzmán, F., Lyamani, H., Fernández-Gálvez, J., Olmo, F. J., and Alados-Arboledas, L.: Retrievals of precipitable water vapor using star photometry: Assessment with Raman lidar and link to sun photometry, Journal of Geophysical Research: 335 Atmospheres, 117, D05 202, https://doi.org/10.1029/2011JD016450, 2012.

Roddier, F.: The Effects of Atmospheric Turbulence in Optical Astronomy, in: Progress in Optics, chap. V, pp. 281–376, Elsevier, https://doi.org/10.1016/S0079-6638(08)70204-X, 1981.

Rousseeuw, P. J. and Croux, C.: Alternatives to the Median Absolute Deviation, Journal of the American Statistical Association, 88, 1273–1283, https://doi.org/10.1080/01621459.1993.10476408, 1993.

340 Rufener, F.: Technique et réduction des mesures dans un nouveau système de photométrie stellaire, Publications de l'Observatoire de Genève, Série A: Astronomie, chronométrie, géophysique, 66, 413–464, http://www.worldcat.org/oclc/491819702, 1964.

Rufener, F.: The evolution of atmospheric extinction at La Silla, Astronomy and Astrophysics, 165, 275–286, http://adsabs.harvard.edu/abs/1986A&A...165..275R, 1986.

Sayer, A. M. and Knobelspiesse, K. D.: How should we aggregate data? Methods accounting for the numerical distributions, with an as-345 sessment of aerosol optical depth, Atmospheric Chemistry and Physics, 19, 15 023–15 048, https://doi.org/10.5194/acp-19-15023-2019, 2019.

Soch, J., Faulkenberry, T. J., Petrykowski, K., Allefeld, C., and McInerney, C. D.: The Book of Statistical Proofs, Open, Zenodo, https://doi.org/10.5281/zenodo.5820411, 2021.

Théorêt, X.: AEROSTAR Conception d'un spectroradiomètre stellaire pour l'étude des aérosols noctures, Ph.D. thesis, Sherbrooke, http: 350 //savoirs.usherbrooke.ca/handle/11143/2335, 2003.

Young, A. T.: Observational Technique and Data Reduction, in: Methods in Experimental Physics, vol. 12, chap. 3, pp. 123–192, Elsevier, https://doi.org/10.1016/S0076-695X(08)60495-0, 1974.